

Energy concentration and positional stability of sonoluminescent bubbles in sulfuric acid for different static pressures

Juan Manuel Rosselló,^{*} Damián Dellavale, and Fabián José Bonetto

Instituto Balseiro-CONICET, Centro Atómico Bariloche, Río Negro, R8402AGP, Argentina

(Received 7 June 2013; published 30 September 2013)

In this study we report several experimental and numerical results on the influence of static pressure (P_0) over the main parameters in *single bubble sonoluminescence* (SBSL), using a sulfuric acid aqueous solution (SA) with low concentrations of argon gas dissolved. Bifrequency driving was used in the experiments to enhance spatial stability of the bubbles. The experimental results were compared with simulations provided by a numerical code that models the radial dynamics of the bubbles. The results showed that an increase on the static pressure of the system shifts the Bjerknes instability threshold, allowing the bubble to access higher acoustic pressures (P_{Ac}). Furthermore, a decrease in the measured ambient radius R_0 and the calculated relative gas concentration c_∞/c_0 were observed. A notorious increment in the bubble collapse violence and energy focusing for P_0 above 1 bar was achieved. These were mainly indicated by the growth of the bubble expansion ratio (R_{max}/R_0), the bubble mechanical energy density, and the maximum bubble wall velocity dR/dt . In agreement with the previous statement, the maximum temperature during the bubble collapse predicted by the model is augmented as well. The use of different harmonics in the ultrasound pressure field regarding energy focusing is also discussed. Finally, we analyzed the stability regions of the R_0 - P_{Ac} parameter space via numerical predictions for P_0 above the measured, identifying the shape instabilities as the main limiting agent to obtain further energy concentration in SA systems at high static pressures.

DOI: [10.1103/PhysRevE.88.033026](https://doi.org/10.1103/PhysRevE.88.033026)

PACS number(s): 78.60.Mq, 43.25.Yw, 43.35.Hl

I. INTRODUCTION

Sonoluminescence is a two-phase phenomenon in which a gas bubble is forced to have a strong spherically converging inertial collapse. The sudden rise in pressure and density within the bubble is sufficiently rapid to almost adiabatically heat the gas until a hot plasma is formed and a very short duration light pulse is emitted [1] (typically 100–300 ps). In contrast with transient cavitation events, a single bubble (SBSL) or a cluster of bubbles is trapped in a region of the fluid by means of an imposed acoustic pressure field. In these cases, the bubbles will undergo strong nonlinear oscillations with the periodicity of the external acoustic field in a regime that can be maintained for several minutes or even hours. In the past eight years, several SBSL experiments were carried out using high viscous and low vapor pressure fluids, such as sulfuric or phosphoric acid aqueous solutions (SA and PA, respectively) with a noble gas dissolved (generally argon or xenon). Employing these kinds of fluids, bubble extinction due to shape instabilities (encountered in water systems) can be avoided [2] and higher acoustic pressures (P_{Ac}^{LF}) can be applied on the bubble. In the case of SA with single frequency and high amplitudes of the excitation signal, the bubbles are usually not spatially fixed but rather describe quasiperiodic orbits around a fixed point. In this context, the limiting agent over the acoustic pressure that might be applied on the bubble is mainly given by the Bjerknes instability [3–5], whose effect is to displace the bubble away from the pressure antinode. Urteaga and Bonetto [6] demonstrated that the orbits could be significantly reduced in size adding a harmonic of the fundamental frequency to the ultrasound excitation signal. The authors also had shown how the use of high-frequency driving (V_{HF}) can act over

the mean equilibrium position of the bubble trapping it in a region of higher P_{Ac}^{LF} . Recently, Dellavale *et al.* [7] performed SBSL experiments using a combination of a strongly degassed Xe-SA85 system and biharmonic driving. The relative small values of the ambient radius obtained ($R_0 \approx 3 \mu\text{m}$) allowed the bubble to access regions of the R_0 - P_{Ac}^{LF} parameter space with high acoustic pressures near the positional stability threshold, attaining high-energy focusing on the bubble collapse.

The effect of the static pressure (P_0) over the intensity of the collapse of a SL bubble has been explored exclusively for water or low viscosity and high vapor pressure aqueous solutions, such as water-glycerin [8,9]. Recently, Gaitan *et al.* [10] and Bader *et al.* [11] performed an extensive experimental study on the influence of ambient pressure and cavitation threshold for transient bubbles in H₂O and D₂O for a range of 1–300 bar in P_0 . The claims about the role of the P_0 on these references are based mainly on the increase of the measured SL light pulse intensity, pulse width, and the amplitude of the shockwave emitted in the bubble collapse. Gordeychuk *et al.* reported an enhanced atomic emission in a series of alkali metals dissolved in various aqueous solutions with augmented P_0 in MBSL [12]. A detailed numerical analysis on SBSL in water by Koch *et al.* [13] shows how the bubble *habitat* is substantially expanded with the use of ambient pressures above atmospheric and low dissolved noble gas concentrations. In the present study, we explored both empirically and *via calculus*, the effects of the static pressure on an Ar-SA85 w/w system. The experiments were performed using low levels of dissolved gas, biharmonic frequency driving, and static pressures in the range of 0.5–2 bar. The main topics discussed are the possibility to use ambient pressures above the atmospheric (925 mbar in Bariloche, Argentina) to enhance the focused acoustic energy on the bubble and their influence over the positional instability (Bjerknes), known to be directly related.

^{*}jrossello@cab.cnea.gov.ar

To the best of our knowledge, there are no previous references of the treated subject using high viscous and low vapor pressure fluids like SA.

II. EXPERIMENTAL SETUP AND METHOD

The resonant vessel used in the experiments was a cylindrical Pyrex flask with a wall thickness of 2.5 mm. The endcaps are slightly oblate to avoid bubbles getting trapped in the upper side of the resonator due to the effect of buoyancy force when the acoustic pressure is not applied. The dimensions of the vessel and the disposition of the drivers are described in Fig. 1(a). The flask has two opposite ports at the top and bottom of the cylinder, both aligned with the cylinder symmetry axis. The bottom port was coupled to a transparent Teflon tube and was used as an auxiliary port to fill the flask with the liquid stored in a second Pyrex reservoir, which was also connected to the static pressure regulation tank. This gas and fluid handling external system allowed us to transfer the liquid to the test cell without exposing it to air. A Können manometer ($-1-3$ bar) was used to measure the static pressure over the gas line. The working fluid in the experiments was a sulfuric acid aqueous solution 85% w/w (SA85) with low concentrations of argon dissolved (typically ~ 8 mbar of pressure head). The main resonance frequency of the apparatus was experimentally determined being approximately $f_0 = 30.35$ kHz. That frequency matches the lowest oscillation mode with a pressure antinode in the geometrical center of the flask [14]. The driving system was built with four equal rectangular cross-section toroidal shaped piezoceramics transducers (PZT) with almost the same radius of curvature of the resonator. Those were attached to the outer cylinder wall using epoxy resin in opposite pairs. The ultrasound pressure signal was measured with a disc-shaped pill PZT, which measures a voltage proportional to the acceleration of the flask wall acting as a microphone (MIC). The sinusoidal driving signal was generated using a system for cocurrent signal synthesis and measurement based on a field programmable gate array (FPGA) technology [15]. The low-frequency signal amplitude (V_{PZT}^{LF}) was increased with a Radio Shack MPA-101 100 W audio amplifier (max. output = $70 V_{Rms}$) and boosted with a tuneable RLC circuit, which permits us to attain typical maximum output values of $90 V_{Rms}$. The high-frequency signal was amplified through a low-distortion amplifier ($Bw = 400$ kHz at $C_L = 2$ nF, max. output = $72 V_{Rms}$) (See Ref. [15] for details). Two opposite PZT drivers were used for the low-frequency signal (f_0). The remaining pair was used for the high-frequency signal, which was set to be an harmonic of f_0 in all the reported measurements. The measured quality factor (Q) for the main resonance of the entire system was approximately 220. Standard Mie scattering technique [16] was used in order to determine the temporal evolution of the bubble radius. The incident light beam for the bubble illumination were generated from a Melles-Griot He-Ne (30 mW nominal power, $\lambda = 632.8$ nm) laser. The scattered light was first collected setting an array of lenses, and then captured with an Oriel 77340 phototube located at scattering angles between 80° to 90° from the forward direction to avoid Mie resonances [Fig. 1(b)]. The measured voltage traces were averaged using the SL light pulse as a temporal reference. The experimental error was reduced

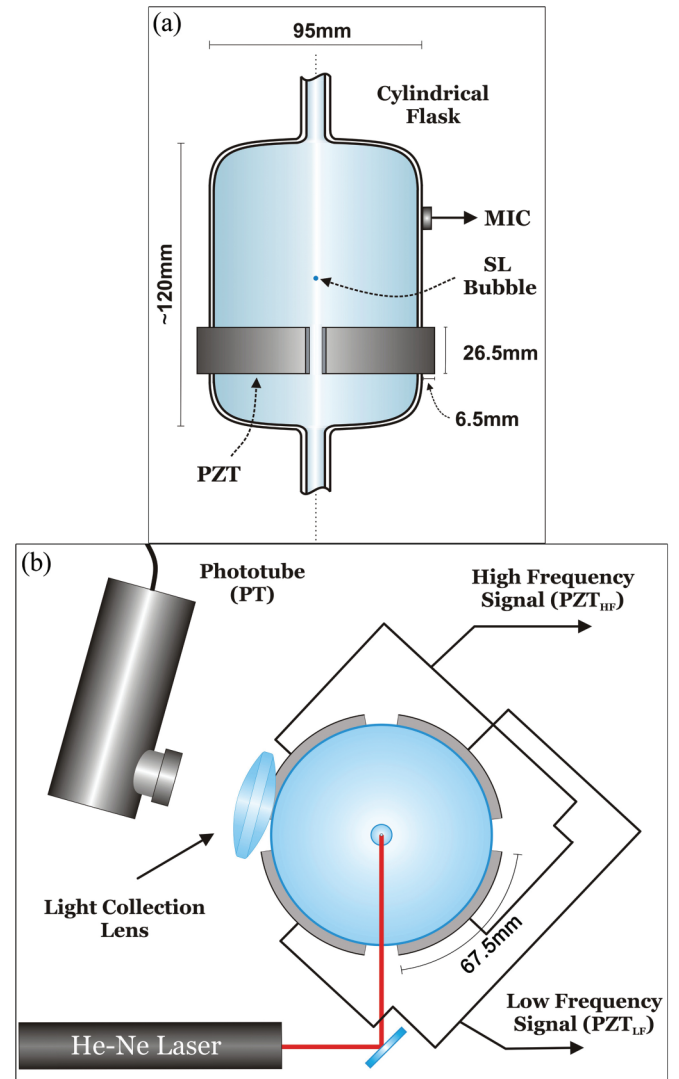


FIG. 1. (Color online) Scheme of the experimental setup. (a) Cylindrical Pyrex resonator. The main resonance frequency was experimentally determined to be about 30.33 kHz, which corresponds to the lowest oscillation mode of the resonator with a pressure antinode in the geometrical center of the flask. (b) Upper view of the acoustic chamber. The Figure details the setup used for the bubble radius temporal evolution measurements via standard Mie scattering technique. An Oriel 77340 phototube was used to acquire the scattered light collected with a Newport KPX142 lens (focal length = 50.2 mm).

by removing the phototube background signal from the traces. The room temperature was controlled to be 300 K in all the measurements. The position, stability, and relative intensity of the studied SL bubbles were evaluated through photographs captured using a Nikon D40x camera.

The measured data was converted to a signal proportional to the bubble radius by means of a fitting process using a numerical model of the bubble dynamics described in Ref. [17]. This model solves the modified Rayleigh-Plesset-Keller equation according to Yasui [18], taking into account evaporation and condensation effects at bubble wall as detailed in Puente *et al.* [17]. All the assumptions in the model have been compared with a Navier-Stokes simulation [20]. The

TABLE I. Physical properties of SA 85% w/w at 300 K.

Vapor pressure [Pa]	5.33
Density [Kg m^{-3}]	1770
Sound velocity [m s^{-1}]	1505
Dynamic viscosity [Pa s]	0.020
Surface tension [N m^{-1}]	0.056
Specific heat [$\text{J kg}^{-1} \text{K}^{-1}$]	1829.2
Thermal conductivity [$\text{W m}^{-1} \text{K}^{-1}$]	0.3578
Refraction index	1.435

heat flux between the gas contents inside the bubble and the liquid were computed based on the thermal boundary layer approximation [20,21]. Specifically, the density and the pressure are taken to be uniform within the bubble. The validity of this assumption has been tested following the work of Lin *et al.* [22] for the experimental data and the simulations. The values of the physical properties of the liquid used in the calculations are summarized in Table I.

III. SBSL PARAMETER EVOLUTION FOR UPSCALED P_0

The effect of the ambient pressure over the main physical parameters involved in SBSL was evaluated studying four series of measurements of the radius temporal evolution of SL bubbles. Each series was performed dissolving different quantities of argon in the SA ($c_\infty/c_0 \sim 4 \times 10^{-3}$, $c_\infty/c_0 \sim 7 \times 10^{-3}$, $c_\infty/c_0 \sim 8 \times 10^{-3}$, and $c_\infty/c_0 \sim 15 \times 10^{-3}$, at a reference ambient pressure of 925 mbar). In detail, the relative concentration (c_∞/c_0) was computed from the numerical fit of the measured bubble dynamics using an equation proposed by Koch *et al.* in Ref. [13], which accounts for the effect of the surface tension and P_0 over the gas concentration c_g . In the experiments, we have set several different values of P_0 in a range between 0.5 and 2 bar via the regulation tank coupled to the resonator system. The limit in the maximum static pressure used was arbitrarily set for safety reasons. In all cases, a fundamental driving frequency near the main resonance of the flask plus a second frequency given by the second, the third, or the sixth harmonic of f_0 , was used to spatially stabilize the bubble (suppressing orbits and avoiding dissolution for bubbles with low R_0) [6,7]. It is worth mentioning that the harmonics did not match in frequency the high-order vibrational modes of the cylinder [14], but the acoustic response was generally adequate when high voltages (about 120 V_p) were applied on the high frequency PZT pair. f_0 was slightly adjusted to improve the harmonic signal without substantially reducing available power from the low-frequency signal. This method proved to be effective because of the low Q value of the fundamental mode ($Q_{LF} \sim 220$). The bubbles were obtained by generating a void in the fluid with the negative pressure phase of the acoustic signal (cavitation bubbles) and immediately after reducing the pressure field amplitude to prevent further cavitation events. In the experiment, the upper bound of P_{Ac}^{LF} that can be delivered to the bubble has two limiting agents: first of all, as V_{PZT}^{LF} was increased the bubble moved away from the pressure antinode once the positional stability threshold was reached; but there was also a cavitation threshold in which multiple bubbles were generated once it was crossed (specially for high-order

harmonics). As Bader *et al.* [11] discussed, high values of P_0 prevent cavitation events in the fluid at elevated acoustic pressures. The authors reported a linear relation between the pressure needed to produce a cavitation bubble and P_0 , using water as the working fluid.

A first insight of how the dynamics of a SL bubble develops with the increase of the static pressure was obtained from the bubble radius temporal evolution (one period of the acoustic field) shown in Fig. 2. In the plot, experimental

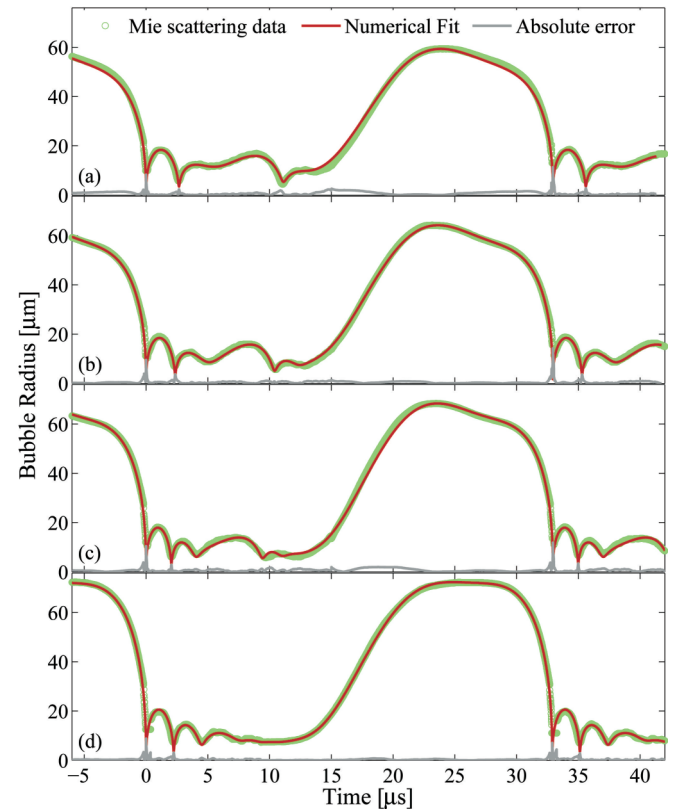


FIG. 2. (Color online) Bubble radius temporal evolution obtained from Mie scattering for argon bubbles in SA85 [Green (gray) circles; the SL light pulses has been removed from the experimental data]. The red (black) curve represents the best numerical fit achieved (minimizing χ^2) and the light gray line the absolute error. The bubbles were driven using a biharmonic signal with $f_0 = 30358.1$ Hz and the third harmonic ($N = 3$). In the presented data the calculated c_∞/c_0 was $\sim 7 \times 10^{-3}$ for $P_0 = 925$ mbar and the bubbles were spatially fixed occupying almost the same position in the resonator (~ 7 mm away from the geometrical center of the cylinder). The experimental data is the average of more than 30 traces of the scattered light. (a) The static absolute pressure in the fluid for this case was (700 ± 15) mbar. The fitted parameters were: bubble ambient radius $R_0 = 10.4 \mu\text{m}$, low-frequency acoustic pressure $P_{Ac}^{LF} = 1.24$ bar, high-frequency acoustic pressure $P_{Ac}^{HF} = 1.35$ bar, and relative phase between the driving frequencies $\varphi = 5.3 \mu\text{s}$. The computed maximum temperature at the instant of collapse was $T_{\text{max}} = 22$ kK. (b) In this case P_0 was (925 ± 15) mbar. $R_0 = 9.8 \mu\text{m}$, $P_{Ac}^{LF} = 1.50$ bar, $P_{Ac}^{HF} = 1.75$ bar, and $\varphi = -5.1 \mu\text{s}$. T_{max} was 28 kK. (c) In this measurement P_0 was (1200 ± 15) mbar. $R_0 = 9.1 \mu\text{m}$, $P_{Ac}^{LF} = 1.86$ bar, $P_{Ac}^{HF} = 2.10$ bar, and $\varphi = -4.5 \mu\text{s}$. T_{max} was 36 kK. (d) P_0 was (1600 ± 15) mbar. $R_0 = 9.4 \mu\text{m}$, $P_{Ac}^{LF} = 2.48$ bar, $P_{Ac}^{HF} = 1.90$ bar, and $\varphi = -3.7 \mu\text{s}$. T_{max} was 43 kK.

results taken using biharmonic driving with the third harmonic ($N = 3$) and four distinct values of P_0 (0.7 bar, 0.925 bar, 1.2 bar, and 1.6 bar) are presented. The SL light pulses were removed from the experimental data to improve the quality of the fitting process (minimizing χ^2). In these measurements, the computed c_∞/c_0 parameter was $\sim 7 \times 10^{-3}$ (at $P_0 = 925$ mbar) and the bubbles were spatially fixed occupying almost the same position in the resonator (~ 7 mm away from the geometrical center of the cylinder). The relative phase between the fundamental frequency and the harmonic in the pressure field (φ) was defined positive when the high frequency was advanced with respect to the low frequency. An excellent agreement between the simulations and the empirically obtained data was found. In Fig. 2, a slight growth in the maximum radius achieved by the bubbles was observed. The latter is a consequence of the increasingly higher acoustic pressures accessible to the bubble (relative to P_0). This fact combined with a reduction in R_0 led to stronger collapses [8]. This particular behavior was also observed in most of the analyzed experimental data. In SBSL using atmospheric static pressure, the ambient radius R_0 is usually interpreted as a measure of mass content in the bubble interior. In the present case where P_0 is varied, the reported values of R_0 are relative to the static pressure used; thus, comparisons must be made only between bubbles with the same P_0 . In Fig. 3, spatially fixed sonoluminescent argon bubbles in SA85 were measured for static pressures of 0.5 bar, 1.2 bar, and 1.6 bar. The bubbles were driven using a biharmonic signal with $f_0 \approx 30.4$ kHz and the second harmonic ($N = 2$). As both P_0 and P_{Ac}^{LF} were increased, there was a notorious growth in the negative slope of the $R(t)$ curves in the moment just previous to the collapse (maximum bubble wall velocity dR/dt), conversely, the decrease in the height of the after bounces imply a reduction in the ambient radius or the relative concentration of dissolved gas (this fact being supported by the numerical model). The slight enhancement of the reachable maximum radius observed when the static pressure was increased was not as rapid as the decrease in R_0 . Finally, Fig. 3 also shows that there was an evident change in the time the bubble was in the expansion phase for unequal static pressures. In low vapor pressure fluids, such as sulfuric acid, this fact must not substantially change the processes occurring in the bubble interior, as happens in water-based systems (e.g., mass diffusion, chemical reactions, ionization of molecules, etc.). In spite of that, it is worth noting that a faster expansion implies a lesser gas being diffused into the bubble interior, which results appropriate for the energy focusing process during the collapse [1,8].

The experimental facts previously illustrated with specific examples were also treated within a global context in Figs. 4 and 5. These charts collect results obtained from the numerical fits for P_{Ac}^{LF} , P_{Ac}^{HF} , dR/dt , the expansion ratio (R_{max}/R_0), the mechanical energy density, the relative gas concentration c_∞/c_0 , and the maximum temperature achieved in the instant of collapse T_{max} . For the plots described in these two figures, the data was coded in a way to discriminate the series with different amounts of gas dissolved in the fluid and also the measurements taken with distinct harmonics in the applied driving signal. Figure 4(a) shows an almost linear relation between the low-frequency acoustic pressure acting over the bubbles (P_{Ac}^{LF}) and P_0 . It is worth noting the change in

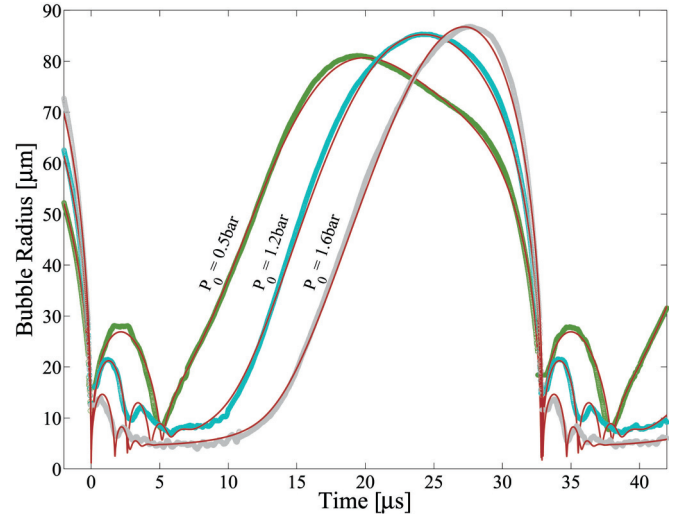


FIG. 3. (Color online) Bubble radius temporal evolution for argon bubbles in SA85 for three distinct P_0 . The green (dark gray), cyan (gray), and light gray dots correspond to the acquired experimental data for 0.5 bar, 1.2 bar, and 1.6 bar respectively. The red (black) curves represent the best numerical fit achieved for each case (minimizing χ^2). The bubbles were driven using a biharmonic signal with $f_0 \approx 30.4$ kHz and the second harmonic ($N = 2$). The low-frequency applied voltage signal had different amplitudes in each case, being of $18.5 V_{Rms}$ for 0.5 bar, $25 V_{Rms}$ for 1.2 bar, and $58 V_{Rms}$ for 1.6 bar; the calculated c_∞/c_0 parameter was $\sim 15 \times 10^{-3}$ for $P_0 = 925$ mbar and the bubbles were spatially fixed. Each measurement is the result of averaging 20 traces of the scattered light. The fitted parameters for each case were: [Green (dark gray) - $P_0 = 0.5$ bar] Bubble ambient radius $R_0 = 14.2 \mu m$, low-frequency acoustic pressure $P_{Ac}^{LF} = 0.96$ bar, high-frequency acoustic pressure $P_{Ac}^{HF} = 1.20$ bar, and relative phase between the driving frequencies $\varphi = 7.0 \mu s$. The computed maximum temperature was 24 kK. [Cyan (gray) - $P_0 = 1.2$ bar] $R_0 = 9.6 \mu m$, $P_{Ac}^{LF} = 2.26$ bar, $P_{Ac}^{HF} = 1.30$ bar, and $\varphi = 8.0 \mu s$. T_{max} was 41 kK. (Light gray - $P_0 = 1.6$ bar) $R_0 = 6.6 \mu m$, $P_{Ac}^{LF} = 3.14$ bar, $P_{Ac}^{HF} = 0.25$ bar, and $\varphi = 4.6 \mu s$. T_{max} was 72 kK.

the slope of the linear arrangement for the data associated with the second harmonic ($N = 2$) and the rest of the data corresponding to the harmonics three or six ($N = 3, 6$). As discussed in the following section, all these bubbles were positionally (Bjerknes) stable, so the difference in the slope must be explained by considering that distinct harmonics have unequal cavitation thresholds. Specifically, higher harmonics were found to have a lower limit on the acoustic pressure that could be delivered to the system, before the fluid begins to cavitate. Considering that the measurements presented were made with dissimilar gas concentrations and biharmonic driving (relative phase and HF amplitude), it was remarkable to find a nearly constant ratio P_{Ac}^{LF}/P_0 . As seen in Fig. 4, P_{Ac}^{LF} and the high-frequency acoustic pressure acting over the bubbles (P_{Ac}^{HF}) had similar amplitudes until they reach a limit value of P_0 in which P_{Ac}^{HF} begins to drop. This correlated well with a similar decay occurring in the HF component of microphone signal; hence, the mentioned decay in P_{Ac}^{HF} must not be interpreted as a change in the HF coupling with the bubble dynamics due to the effect of P_0 , as the plot might suggest. Figure 4(b) presents the maximum bubble wall velocity (dR/dt)

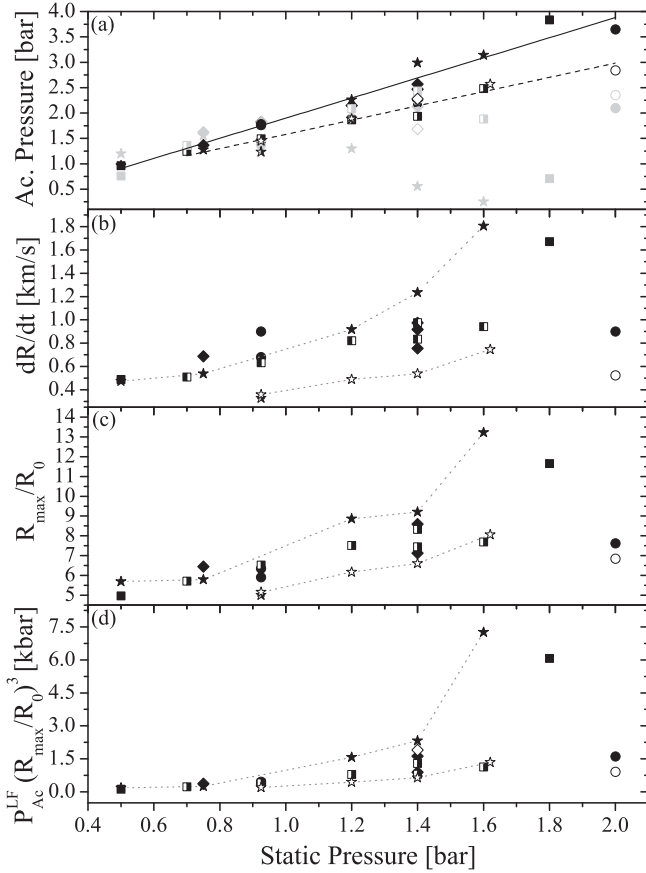


FIG. 4. Fitted parameters of the experimental data as a function of P_0 for four distinct data series. The symbols in the graphs were coded as follows. The squares, circles, stars, and rhombus represent each data series with $c_\infty/c_0 \sim 7 \times 10^{-3}$, $c_\infty/c_0 \sim 8 \times 10^{-3}$, $c_\infty/c_0 \sim 15 \times 10^{-3}$, and $c_\infty/c_0 \sim 4 \times 10^{-3}$, respectively, taken at $P_0 = 925$ mbar. In the figures, the filled markers indicate measurements made with the second harmonic of the fundamental driving frequency ($f_0 \sim 30356$ Hz), the half-filled markers correspond to measurements made applying the third harmonic ($N = 3$), and the unfilled markers are associated with the sixth harmonic ($N = 6$). The dotted gray lines connecting the star markers are drawn to ease the visualization of the data measured using $c_\infty/c_0 \sim 15 \times 10^{-3}$. The uncertainty in P_0 was $\Delta P_0 = 15$ mbar. The relative error of the other physical quantities shown are: $\Delta P_{Ac}^{LF} = 1\%$, $\Delta P_{Ac}^{HF} = 3\%$, $\Delta(dR/dt) = 2.8\%$, $\Delta(R_{max}/R_0) = 1.5\%$ and $\Delta(P_{Ac}^{LF}(R_{max}/R_0)^3) = 2.5\%$. (a) Acoustic pressures (P_{Ac}^{LF} and P_{Ac}^{HF}) acting on the bubbles as a function of P_0 . The solid line is a linear fit of the filled markers ($P_{Ac}^{LF} = 1.98P_0 - 0.04$; $r^2 = 0.966$) and the dashed line is a fit of the measurements taken using harmonics $N = 3$ and $N = 6$ ($P_{Ac}^{LF} = 1.40P_0 + 0.17$; $r^2 = 0.938$). Here, the light gray markers signify the high-frequency acoustic pressure (P_{Ac}^{HF}) associated with the data points with the same marker in black. (b) Maximum bubble wall velocity dR/dt vs. P_0 . It grows rapidly with an increment of P_0 as can be seen from the plot. (c) R_{max}/R_0 ratio vs. P_0 . This parameter, related with the strength of collapse, grows with P_0 in a quadratic fashion doubling its value in a raise of 1 bar (0.5 to 1.5 bar). (d) Mechanical energy density for distinct P_0 . According to the nonlinear evolution of the expansion ratio, this quantity can be enhanced in a factor 25 augmenting P_0 in 1 bar (0.5 to 1.5 bar).

as a function of P_0 . The bubble interface velocity taken just before the minimum radius is a direct measurement of the

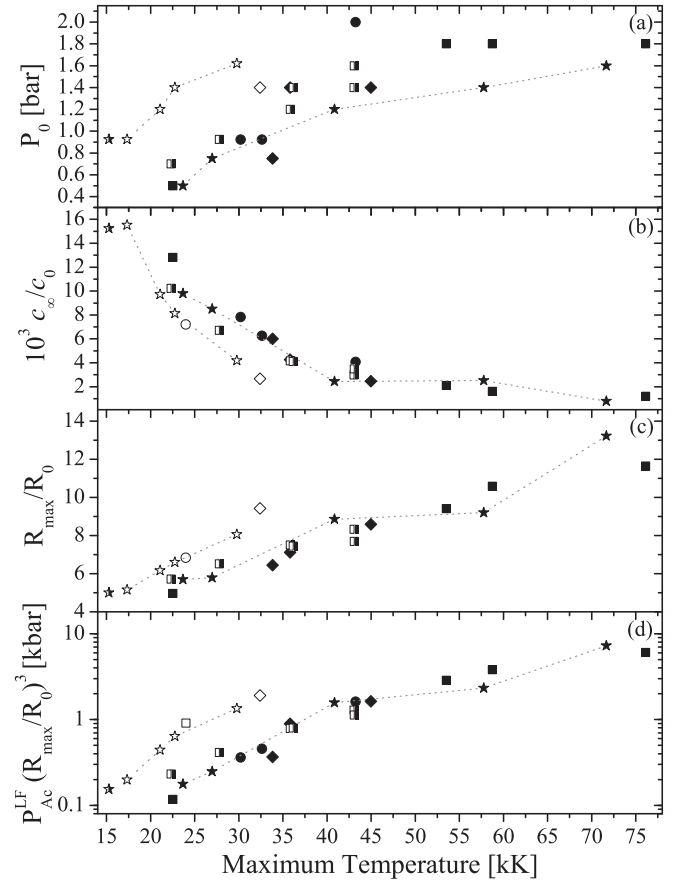


FIG. 5. Fitted parameters of the experimental data as a function of the maximum temperature achieved in the instant of collapse (T_{max}). The symbols in the graphs are coded in the same fashion explained in the legend of Fig. 4. The uncertainty in P_0 was $\Delta P_0 = 15$ mbar. The relative error of the other physical quantities shown are: $\Delta(c_\infty/c_0) = 4\%$, $\Delta(R_{max}/R_0) = 1.5\%$, $\Delta(P_{Ac}^{LF}(R_{max}/R_0)^3) = 2.5\%$, and $\Delta(T_{max}) = 3\%$. (a) Static pressure vs. T_{max} . The dotted gray lines connecting the star markers are drawn to ease the visualization of the data measured using $c_\infty/c_0 \sim 15 \times 10^{-3}$. The second harmonic of f_0 is the most satisfactory to achieve high-energy focusing (in the context of this particular experiment). (b) c_∞/c_0 related with the maximum temperature. This figure shows that large T_{max} could be obtained using low dissolved gas concentration and also shows the decay occurring in c_∞/c_0 with augmented P_0 (or the growth of c_0 according to Henry's Law). (c) R_{max}/R_0 as a function of T_{max} . The relation between these two variables can be approximated in a linear fashion with different slopes for distinct harmonics. (d) Relation between the mechanical energy density for P_{Ac}^{LF} and the T_{max} obtained by means of gas kinetic theory. This plot shows that for $N = 6$, the mechanical energy that was actually transformed into heat was found to be less than the one for lower harmonics ($N = 2, 3$).

violence of the collapse. The magnitude of dR/dt grows rapidly with an increment of P_0 in an almost quadratic fashion. This can be tripled increasing P_0 in 1 bar (from 0.5 to 1.5 bar). The expansion ratio (R_{max}/R_0) and the mechanical energy density [$P_{Ac}^{LF}(R_{max}/R_0)^3$] are detailed in Figs. 4(c) and 4(d). Both parameters depend exclusively on the bubble dynamics and are also strong indicators of the strength of the inertial collapse. The results revealed that the linear growth in P_{Ac}^{LF} and P_0 leads to a nonlinear increase in the strength of collapse,

and ergo the focused energy. The magnitude of the expansion ratio could be doubled [filled stars in Fig. 4(c)] and P_{Ac}^{LF} almost tripled [stars in Fig. 4(d)] increasing P_0 just 1 bar (from 0.5 to 1.5 bar); thus, the acoustic energy density could be enhanced by a factor of 25. Additionally, Fig. 5 relates the quantities in Fig. 4 (and c_∞/c_0) to the maximum temperature achieved in the instant of collapse T_{max} , computed using gas kinetic theory. The subplot (a) in Fig. 5 shows a nonlinear increase in the reachable temperatures with P_0 . Furthermore, this plot suggests that for even higher static pressures it is possible to produce increasingly large ΔT_{max} augmenting P_0 by the same ΔP_0 . Considering the existing limiting agents like bubble breakup, diffusive instability, and positional instability, the latter statement is not valid for pressures approximately 1 bar above the measured range, as discussed with more detail in Sec. IV. Figure 5(b) relates the adimensional parameter c_∞/c_0 with T_{max} . This figure shows that large T_{max} could be obtained using low dissolved gas concentration and also displays the decay occurring in c_∞/c_0 with augmented P_0 (or the growth of c_0 according to Henry's Law). This decay was expected since c_∞ represents the concentration of dissolved gas in the fluid, which must not change considerably during the measurement process. The observed low c_∞/c_0 values are also relevant in the spatial stability of the bubbles as Dellavale *et al.* have previously shown in Ref. [7]. Low values of c_∞/c_0 favors the removal of bubble orbits, a fact that has been noticed during the present experiments. Figure 5(c) shows the fitted expansion ratios R_{max}/R_0 as a function of T_{max} . The relation between R_{max}/R_0 and T_{max} can be approximated by a linear function with different slopes for distinct harmonics. Finally, Fig. 5(d) shows values of the mechanical energy density and the maximum temperature obtained by means of gas kinetic theory. Specifically, we found through a nonlinear curve fit of the experimental data that the mechanical energy density evolves approximately as a power relation $(T_{max})^{3.5}$ for the data with $N = 6$, and $(T_{max})^{2.8}$ for $N = 2, 3$. The latter imply that, to double a given value of T_{max} , an increment of 11 times of $P_{Ac}^{LF} \cdot (R_{max}/R_0)^3$ is needed using the sixth harmonic of f_0 , while a factor 7 is needed for $N = 2$. Therefore, we can conclude that the mechanical energy, which was actually transformed into heat for $N = 6$, was found to be less than the one for lower harmonics ($N = 2, 3$).

Comparing experimental data from the same series of measurements, we observed that the values of R_{max} attainable for bubbles driven with $N = 6$ and $N = 2$ were significantly dissimilar, the latter being approximately 60% larger. This clearly explains the mentioned change in the expansion ratio and the maximum temperature for the second and the sixth harmonics of f_0 . Furthermore, the higher cavitation threshold found for $N = 2$ permitted the bubbles to achieve elevated amplitudes of acoustic pressure without generating multiple cavitation events. According to the values of R_{max}/R_0 , dR/dt , T_{max} and the mechanical energy density obtained from the fits, the second harmonic of f_0 was the most satisfactory to achieve high-energy focusing. However, it is worth noting that it was also found to be the worst harmonic to use in terms of positional, spatial, and shape stability; thus, further analysis must be performed to establish solid conclusions about this topic. The maximum temperature obtained in this study was approximately 76 kK ($R_{max}/R_0 = 11.7$ and

$dR/dt = 1.7$ km/s) for a bubble driven with $N = 2$ and 1.8 bar of static pressure.

A high proportion of the current literature about SBSL reports experimental results in terms of the amplitude of the SL light pulse. The light intensity emitted by the SL bubbles must not be related only to the strength of collapse, since it also depends on the bubble volume through the ambient radius R_0 (correlated with the concentration of gas dissolved in the fluid). Larger bubbles produce larger and longer SL flashes, which do not strictly imply a growth in the strength of collapse and the energy concentration over the bubble, as demonstrated by Hopkins *et al.* in Ref. [3]. As an example of this phenomenon, using an excitation signal with $f_0 \approx 30.4$ kHz and $N = 2$, we measured by means of a NIST calibrated detector (Newport 840-C) the light intensity (referred to $\lambda = 400$ nm) emitted from two distinct bubbles, whereas the first one had parameters: $P_0 = 0.75$ bar; $R_0 = 15.2$ μm ; $P_{Ac}^{LF} = 1.28$ bar; $P_{Ac}^{HF} = 1.55$ bar; $R_{max}/R_0 = 5.8$, and $T_{max} \sim 27$ kK; and the second: $P_0 = 1.6$ bar; $R_0 = 6.5$ μm ; $P_{Ac}^{LF} = 3.14$ bar; $P_{Ac}^{HF} = 0.25$ bar; $R_{max}/R_0 = 13.2$, and $T_{max} \sim 72$ kK. The light captured from the second bubble was notoriously dimmer, being about 10% of the light emitted by the first one.

IV. EFFECT OF P_0 OVER THE BUBBLE HABITAT

The notion of a *bubble habitat* was introduced in works performed by Koch *et al.* [13] and Lauterborn *et al.* [23] and refers to regions in some two-dimensional space of parameters where positionally and spherically stable, nondissolving bubbles can exist. In Sec. III, we discussed the changes of several physical parameters of interest (P_{Ac}^{LF} , P_{Ac}^{HF} , R_{max}/R_0 , dR/dt , c_∞/c_0 , and T_{max}), related with the modification of P_0 in the experiments. Additional information beyond the presented particular cases can be deduced by placing them in the context of a R_0 - P_{Ac}^{LF} plane and further analyzing the boundaries of the bubble habitat via calculus using a numerical model. Particular attention will be given to the effect of P_0 in the Bjerknes instability. This threshold has proven to be the principal frontier to reach higher P_{Ac}^{LF} and energy concentrations in SA85 systems [5].

In Fig. 6, we present phase space diagrams for the experimental data points discussed in Fig. 2. In these diagrams, the frontier between the positionally stable and unstable regions is determined by a null value in the computed Bjerknes force. In order to define the boundary of the bubble habitat, we also included the Blake threshold, the Parametric instability (PI), and the Rayleigh-Taylor instability (RTI) thresholds. For the latter, we considered a perturbation in the bubble surface with the mode $n = 2$ and an initial amplitude of 1 nm taken at the instant with null bubble interface velocity and maximum radius [$dR(t_i)/dt = 0$; $R(t_i) = R_{max}$] [17]. The regions with diffusive stability in the maps can be established with the aid of the constant c_∞/c_0 lines, the zones being stable where these lines have a positive slope [$\partial(c_\infty/c_0)/\partial R_0|_m > 0$]. In agreement with the numerical calculations, the experimental data points were found to be located over positional-, diffusive-, and shape-stable regions of the maps. It is worth noting that as the static pressure is increased there is a shift of both Bjerknes and Blake thresholds to regions of higher acoustic pressures. The difference in the rate of change between these

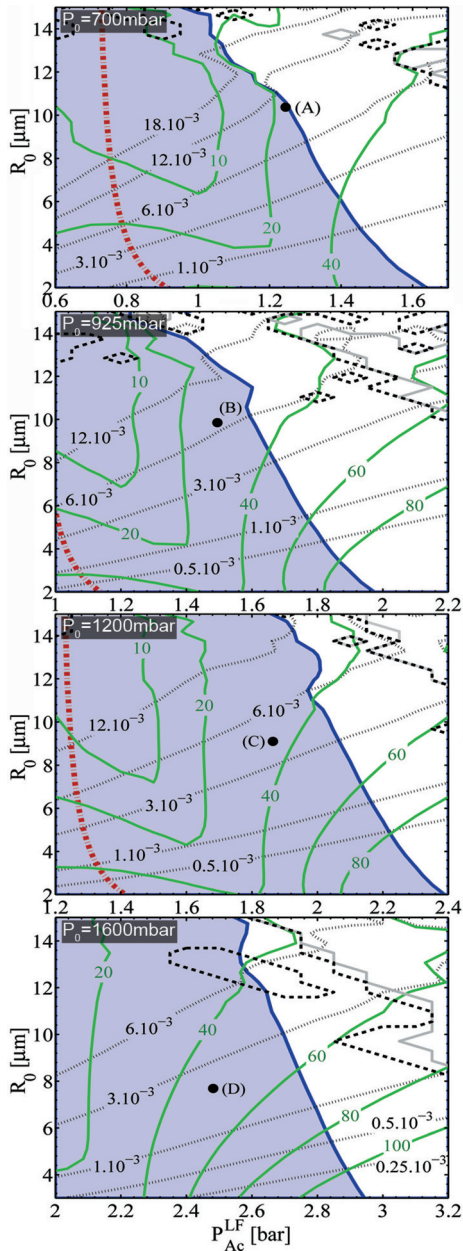


FIG. 6. (Color online) Computed R_0 - P_{Ac}^{LF} parameter map for the Ar-SA85 system for the case of a bifrequency driving ($f_0 \approx 30.36$ kHz, $N = 3$) and different static pressures. The solid blue (black) line is the Bjerknes stability threshold ($F_{Bj} = 0$). This line delimits the positionally stable region of the map [shaded in light blue (gray)] and the unstable region (uncolored). In each subplot, the parameters for the calculations has been set in order to match the fitted parameters of the experimental data points (\bullet) shown in Fig. 2. The label between parenthesis correlates with the $R(t)$ in Fig. 2. The thick dash-dotted red (black) line is the Blake threshold. The solid line in light gray is the Rayleigh-Taylor shape instability for the mode $n = 2$. The thick dashed line (black) corresponds to the parametric shape instability threshold. In the latter two curves, the stable region is always below the lines, or outside the closed curves for the “instability islands” in the plots. The green (gray) solid curves are the contours of constant T_{max} (in units of kK) and the thin dotted curves (black) are the contours of constant c_∞/c_0 . The graphs demonstrate that there is an expansion of the bubble habitat as the static pressure of the system is increased.

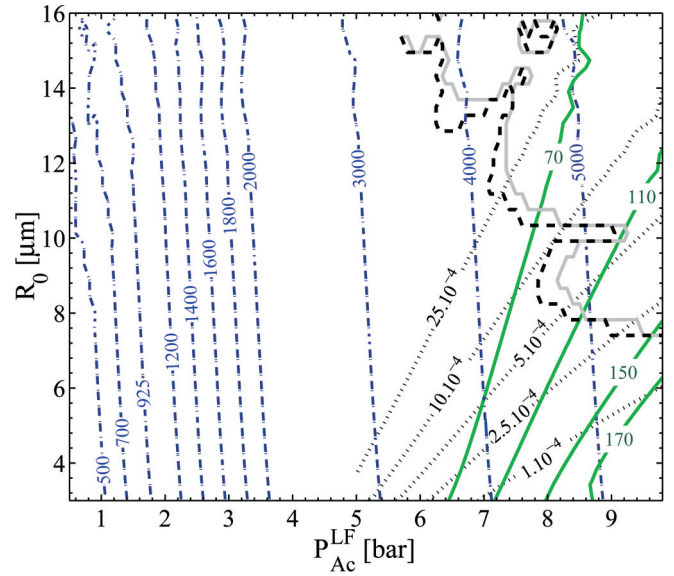


FIG. 7. (Color online) Computed Bjerknes stability threshold for different static pressures. In all the presented data, the parameters used in the numerical model corresponded to the case discussed in the legend of Fig. 2(d) ($f_0 \approx 30.36$ kHz, $N = 3$, $P_{Ac}^{HF} = 1.9$ bar, and $\varphi = -3.7$ μ s). The dash-dotted blue (black) lines are the Bjerknes stability threshold ($F_{Bj} = 0$) with a label indicating the static pressure used for the computation of each curve in units of mbar. The stable Bjerknes zone is always to the left of each curve. The light gray solid line is the Rayleigh-Taylor shape instability for the mode $n = 2$ and an initial perturbation of 1 nm for the case with $P_0 = 5$ bar. The thick dashed line (black) corresponds to the parametric shape instability threshold for the case with $P_0 = 5$ bar. In the latter two curves, the stable region is always below the lines. The green (gray) solid curves are the contours of T_{max} (in units of kK) and the thin dotted curves (black) are the contours of constant c_∞/c_0 for the case with $P_0 = 5$ bar. As the static pressure is increased, there was a shift of both Bjerknes threshold and Blake threshold (not shown) to regions of higher acoustic pressures. For the maximum computed static pressure in the plot, the numerical model predicted that a bubble with ambient radius of ~ 4 μ m could achieve a maximum temperature of approximately 170 kK.

two boundaries resulted in an extension of the bubble habitat as previously reported by Kock *et al.* [13]. In contrast, the shape stability curves approached to the $F_{Bj} = 0$ frontier with the increasing static pressure until there was an overlap between them for large values of R_0 , as shown in the map corresponding to the case with $P_0 = 1600$ mbar (Fig. 6). Furthermore, Fig. 7 shows calculations for the R_0 - P_{Ac}^{LF} plane for an extended range in P_0 of 0.5 to 5 bar. In these calculations, the dynamical parameters in the model were set to be the same as the experimental data point of Fig. 2(d) ($f_0 \approx 30.36$ kHz, $N = 3$, $P_{Ac}^{HF} = 1.90$ bar, and $\varphi = -3.7$ μ s). This figure shows in detail the mentioned shift in the Bjerknes frontier. Taking the average low-frequency acoustic pressure in which $F_{Bj} = 0$ for ambient radius from 12 to 6 μ m (where most of the measured bubbles reside), a linear relation connecting the mean value of $P_{Ac}^{LF}|_{F_{Bj}=0}$ and P_0 could be established ($P_{Ac}^{LF}|_{F_{Bj}=0} = 1.74P_0 - 0.06$; $r^2 = 0.999$, obtained via standard fitting procedure). In regards to energy focusing, the numerical model predicted that a bubble with ambient radius of ~ 4 μ m

can achieve a maximum temperature of approximately 170 kK for the highest computed static pressure in Fig. 7 (5 bar). Similar calculations for $P_0 = 15$ bar indicates that, for this particular set of parameters, only bubbles with R_0 below $3 \mu\text{m}$ can avoid bubble rupture near the positional stability line of the map, reaching an approximately T_{max} of 240 kK. Otherwise, bubbles with ambient radius above that value were found to be spherically stable for $P_{\text{Ac}}^{\text{LF}}$ approximately 4 bar below $P_{\text{Ac}}^{\text{LF}}|_{F_{\text{Bj}}=0}$, reaching similar temperatures to the ones attainable with 5 bar of P_0 . The overlap of the spatially stable and the shape unstable regions found for elevated P_0 suggests that the attainable energy focusing using this strategy would be limited by the bubble breakup instead of the positional instability.

V. CONCLUSIONS

The experimental data and the calculations reported in this study revealed several effects related to the use of static pressures above the atmospheric in SBSL. We summarize as follows the main facts encountered: (1) the low-frequency acoustic pressures accessible by the bubble increased in a nearly linear fashion with P_0 . An increment of 1 bar in P_0 (from 0.5 to 1.5 bar) results in a twofold increase of the amplitude of $P_{\text{Ac}}^{\text{LF}}$. In the experiment, high values of P_0 prevented multiple cavitation events in the fluid at elevated acoustic pressures; (2) statement (1) is supported by the Bjerknes instability threshold shift to regions of the R_0 - $P_{\text{Ac}}^{\text{LF}}$ parameter space where low R_0 and higher $P_{\text{Ac}}^{\text{LF}}$ were accessible to the bubble; (3) the values of the expansion ratio R_{max}/R_0 and the maximum bubble wall velocity dR/dt , which are directly related to the strength of the inertial collapse, could almost be tripled by incrementing P_0 in 1 bar (0.5 to 1.5 bar); (4) the relative concentration ratio c_{∞}/c_0 was extremely reduced (because of

the increase in c_0 according to Henry's Law). This implies a minor quantity of molecules absorbing energy in the bubble interior during the heating process [23] (this being closer to the situation of a Rayleigh collapse of an empty cavity), and besides playing an important role in the pseudo-orbits suppression; (5) by combining (1) and (3), it was possible to estimate an increase in the mechanical energy density of the bubble by a factor 25, which resulted in a raise of T_{max} by approximately a factor of 2.6. The experimental results showed that for $N = 6$, the mechanical energy that was actually transformed into heat was found to be less than the one for lower harmonics ($N = 2, 3$).

The performed calculations of the R_0 - $P_{\text{Ac}}^{\text{LF}}$ parameter space revealed that there is an expansion of the bubble habitat as the static pressure is incremented. In the set of measurements treated in this study, we were able to trap bubbles with temperatures of about 76 kK with $P_0 = 1.8$ bar; meanwhile, the typical values obtained at atmospheric pressure (925 mbar) were around 28 kK. Therefore, we believe that the use of even higher static pressures is a promising technique to reach enhanced energy focusing and maximum temperatures in SBSL. However, as discussed in Sec. IV, the next limiting factor to this aim would be given by the bubble breakup indicated by the numerical model for high static pressures (P_0 above ~ 10 bar in the studied case). In this case, bubble extinction could be avoided only by bubbles with low R_0 and extremely low gas content.

ACKNOWLEDGMENTS

We acknowledge Enrique Aburto who fabricated the Pyrex vessels used in the experiments. We also thank Raúl Urteaga and Pablo García Martínez for helpful discussion. J.M.R. and D.D. were supported by CONICET.

-
- [1] T. Matula, *Philos. Trans. R. Soc. London A* **357**, 225 (1999); *J. Acoust. Soc. Am.* **114**, 775 (2003).
 - [2] R. Urteaga, D. Dellavale, G. Puente, and F. Bonetto, *J. Acoust. Soc. Am.* **124**, 1490 (2008).
 - [3] S. D. Hopkins, S. J. Putterman, B. A. Kappus, K. S. Suslick, and C. G. Camara, *Phys. Rev. Lett.* **95**, 254301 (2005).
 - [4] I. Akhatov, R. Mettin, C. D. Ohl, U. Parlitz, and W. Lauterborn, *Phys. Rev. E* **55**, 3747 (1997).
 - [5] R. Urteaga, D. H. Dellavale, G. F. Puente, and F. J. Bonetto, *Phys. Rev. E* **76**, 056317 (2007).
 - [6] R. Urteaga and F. J. Bonetto, *Phys. Rev. Lett.* **100**, 074302 (2008).
 - [7] D. Dellavale, L. Rechiman, J. M. Rosselló, and F. Bonetto, *Phys. Rev. E* **86**, 016320 (2012).
 - [8] M. Dan, J. D. N. Cheeke, and L. Kondic, *Phys. Rev. Lett.* **83**, 1870 (1999).
 - [9] G. E. Vazquez and S. J. Putterman, *Phys. Rev. Lett.* **85**, 3037 (2000).
 - [10] D. F. Gaitan, R. A. Tessien, R. A. Hiller, J. Gutierrez, C. Scott, H. Tardif, B. Callahan, T. J. Matula, L. A. Crum, C. C. Church, and J. L. Raymond, *J. Acoust. Soc. Am.* **127**, 3456 (2010).
 - [11] K. B. Bader, J. L. Raymond, J. Mobley, C. C. Church, and D. F. Gaitan, *J. Acoust. Soc. Am.* **132**, 728 (2012); K. B. Bader *et al.*, **132**, 2286 (2012).
 - [12] T. V. Gordeychuk and M. V. Kazachek, *Opt. Spektrosk.* **106**, 238 (2009).
 - [13] P. Koch, T. Kurz, U. Parlitz, and W. Lauterborn, *J. Acoust. Soc. Am.* **130**, 3370 (2011).
 - [14] P. Birkin, T. G. Leighton, J. F. Power, M. D. Simpson, A. M. L. Vinçotte, and P. F. Joseph, *J. Phys. Chem. A* **107**, 306 (2003).
 - [15] D. Dellavale, Ph.D. thesis, Balseiro Institute 2012; D. Dellavale, M. Sonnaillon, and F. Bonetto, *IEEE 4th Southern Conference on Programmable Logic* (IEEE, Piscataway, NJ, 2008), p. 269.
 - [16] R. G. Holt and L. A. Crum, *Appl. Opt.* **29**, 4182 (1990); B. P. Barber and S. J. Putterman, *Phys. Rev. Lett.* **69**, 3839 (1992).
 - [17] G. F. Puente, Ph.D. thesis, Balseiro Institute, 2005.
 - [18] K. Yasui, *Phys. Rev. E* **63**, 035301 (2001).
 - [19] G. F. Puente, R. Urteaga, and F. J. Bonetto, *Phys. Rev. E* **72**, 046305 (2005).

- [20] G. F. Puente, P. García-Martínez, and F. J. Bonetto, *Phys. Rev. E* **75**, 016314 (2007).
- [21] R. Toegel, B. Gompf, R. Pecha, and D. Lohse, *Phys. Rev. Lett.* **85**, 3165 (2000).
- [22] H. Lin, B. D. Storey, and A. J. Szeri, *J. Fluid Mech.* **452**, 145 (2002).
- [23] W. Lauterborn, and T. Kurz, *Rep. Prog. Phys.* **73**, 106501 (2010); W. Lauterborn, T. Kurz, P. Koch, M. Alizadeh, H. Söhnholz, and D. Schanz, in *Proceedings of the 19th International Symposium on Nonlinear Acoustics: State-Of-The-Art and Perspectives: ISNA19, Tokyo, Japan, 2012*, edited by T. Kamakura and N. Sugimoto (American Institute of Physics, New York, 2012), p. 95.